Virtual Arm Impedance Emulation and Stability Improvement in Modular Multilevel Converters

Ye Zhu, *Graduate Student Member, IEEE*, Shan Jiang, *Graduate Student Member, IEEE*, Josep Pou, *Fellow, IEEE*, and Georgios Konstantinou, *Senior Member, IEEE*

***Abstract*—The arm impedance in a modular multilevel converter (MMC) influences both the internal dynamics and the converter impedance, significantly impacting the overall system stability. This article proposes a damping method with virtual arm impedance to suppress the small-signal oscillations caused by impedance interactions and improve the MMC stability. The virtual arm impedance, including both a resistance and a reactance component, is emulated based on the common-mode (CM) second-harmonic circulating current, which is injected to optimize the capacitor voltages of MMCs. Different from existing virtual impedance methods, the steady-state operation of the MMC is not influenced by the CM virtual arm impedance. It is shown that the virtual reactance of the same impedance has a better damping effect, compared with the virtual resistance. Selection guidelines of virtual reactance are also provided considering both the stability margin and dynamic performance. Moreover, the stability improvement is quantified by a stability boundary map and validated by real-time grid interaction studies and experimental results. This paper is accompanied by a video file demonstrating the experimental validation of the proposed virtual arm impedance emulation methods.**

***Index Terms*—Active damping, modular multilevel converter (MMC), small-signal stability, virtual impedance.**

I. Introduction

MODULAR multilevel converters (MMCs) are widely used in power systems thanks to their salient features of high modularity, high efficiency, and high power quality [1], [2]. Stability of a grid-connected MMC, which can be evaluated by impedance-based analysis methods, is critical for the safe operation of power systems [3], [4]. As the grid stiffness is decreasing with the increasing integration of power converters [5], [6], a damping method is needed to shape the MMC impedance and enhance the small-signal stability of an MMC-connected system.

Passive damping methods are typically implemented by selecting a proper arm inductance, which can regulate the internal circulating current and suppress small-signal oscillations. A parallel capacitor can be integrated in the arm through a tap of the MMC arm inductor to suppress the second-order harmonics in the circulating current [7], [8]. An arm inductance selection guideline is proposed in [9] to eliminate the circulating current harmonics at the switching frequency, when the second-order harmonics is reduced by circulating current suppression control (CCSC). The high-frequency negative damping effects and the corresponding oscillations generated by the control time delay in MMCs can be mitigated by a passive resistor–capacitor damper [10]. Both first-order and second-order dampers can eliminate the negative damping effect. The damping frequency range of passive damping methods is constant and determined by the specific filter parameters, thus the damping effects will be undermined when the grid conditions change.

The stability of a grid-connected MMC can also be improved by active damping methods. The impedance shaping effects and the corresponding stability boundaries of controller gains have been investigated in the literature. The optimal design of controller gains within their boundaries can maximize the system stability margin [11]. In [3], the impact of the ac voltage proportional gain on the MMC stability is analyzed, and the optimal value range is proposed considering both converter impedance interactions and control dynamics. The feedforward gains in output current and circulating current controllers are optimized to suppress the high-frequency resonance [12]. In [13], adaptive notch filters are adopted to mitigate the high-frequency resonance. The filter parameters are tuned with the online estimated resonance frequency.

Modification of control structure is an effective approach to shape the MMC impedance and enhance the system stability [14], [15], [16], [17], [18]. Combining an integral part with a proportional-resonant regulator in the output voltage controller in a standalone MMC can lower the low-frequency impedance magnitude to avoid impedance interactions between the MMC and the power grid [14]. A broadband impedance shaping method for the MMC-based static synchronous compensator is proposed in [15] to generate a virtual parallel impedance at the ac-side terminal. By introducing a damping controller to generate a compensation voltage by oscillatory dc current, a virtual impedance is emulated to suppress the instability of the dc grid [16], [17]. Considering the coupling among the dc system, positive and negative sequences in the ac system of an MMC, virtual resistance control can be simultaneously added in both dc and ac sides [18]. The virtual resistance is emulated by

Manuscript received 21 September 2023; revised 21 December 2023; accepted 2 January 2024. Date of publication 9 January 2024; date of current version 16 February 2024. Recommended for publication by Associate Editor E. Babaei. *(Corresponding author: Ye Zhu.)*

Ye Zhu, Shan Jiang, and Georgios Konstantinou are with the School of Electrical Engineering and Telecommunications, University of New South Wales, Sydney, NSW 2052, Australia (e-mail: ye.zhu1@unsw.edu.au; shan.jiang4@unsw.edu.au; g.konstantinou@unsw.edu.au).

Josep Pou is with the School of Electrical and Electronic Engineering, Nanyang Technology University, Singapore 639798 (e-mail: josep.pou@ieee.org).

This article has supplementary material provided by the authors and color versions of one or more figures available at https://doi.org/10.1109/TPEL.2024.3351890.

Digital Object Identifier 10.1109/TPEL.2024.3351890

introducing a feedforward proportional component of the output current to the modulation signal, where the proportional gain equals to the virtual resistance magnitude. The output current based virtual impedance emulation can be implemented in both two-level converters and MMCs. However, the inclusion of virtual output impedance has adverse impacts of deviating the converter power from the preset operation point [18]. Additional control loops are required to compensate the voltage drop across the virtual resistance and mitigate the static error in the output power [19].

As the internal dynamics of an MMC have significant impact on the impedance response, the active damping compensation components can be calculated based on the internal parameters in the MMC [20], [21], [22], which is not an option in two-level converters. The differential-mode (DM) internal dynamics are directly related to the output performance of the MMCs. In [20], the DM damping component is determined by the capacitor voltages feedforward control to regulate the DM output voltage and maintain stability. A disturbance equation, indicating interaction between the external output current and internal DM submodule capacitor voltage ripples, is derived in [21]. An oscillation mitigation method in the dq frame based on the disturbance observer is also proposed. In addition to the capacitor voltage, circulating current is an important variable related to the internal dynamics. In [22], a virtual arm resistance control is implemented by the circulating current feedback with a proportional regulator. A modulation component generated by the circulating current controller is added to the DM fundamental modulation voltage, which suppresses the low-frequency resonance peak in the MMC impedance to improve system stability, when CCSC is adopted.

Circulating current injection methods based on instantaneous methods are proposed in [23] to reduce the submodule capacitor voltage ripples. The circulating current reference is calculated by the instantaneous output current and modulation signals, which avoids the use of large look-up tables and facilitates the implementation of circulating current control. However, it is observed in [24] that the controller couplings in the circulating current injection methods compromise the system stability, and a damping method is required.

To guarantee the system stability while maintaining the advantages of the circulating current injection methods, this article proposes a virtual arm impedance emulation method by introducing common-mode (CM) compensation terms in the insertion index. The virtual arm impedance is generated with the help of the injected circulating current harmonics instead of the dc component, thus the power balance between dc and ac sides remains intact. With the combination of the virtual resistance and reactance, the introduced arm impedance can be controlled with flexible magnitude and phase. The stability improvement capability of the virtual impedance is quantified by a stability boundary map, which can help to facilitate stability-oriented controller design in MMCs.

The rest of this article is organized as follows. In Section II, the sequence impedance model of MMC with instantaneous circulating current injection methods is reviewed, and their stability limits are discussed. The proposed active damping methods, including the realization of both virtual and virtual reactance, are analyzed in Section III. The impedance model of the damping methods is also developed and validated. The damping effects of the proposed damping methods are compared in Section IV with real-time simulation. The damping parameter selection procedure and the improved stability boundaries are also provided. Section V presents experimental results to validate and compare the damping effect of the proposed virtual arm impedance. Finally, Section VI concludes this article.

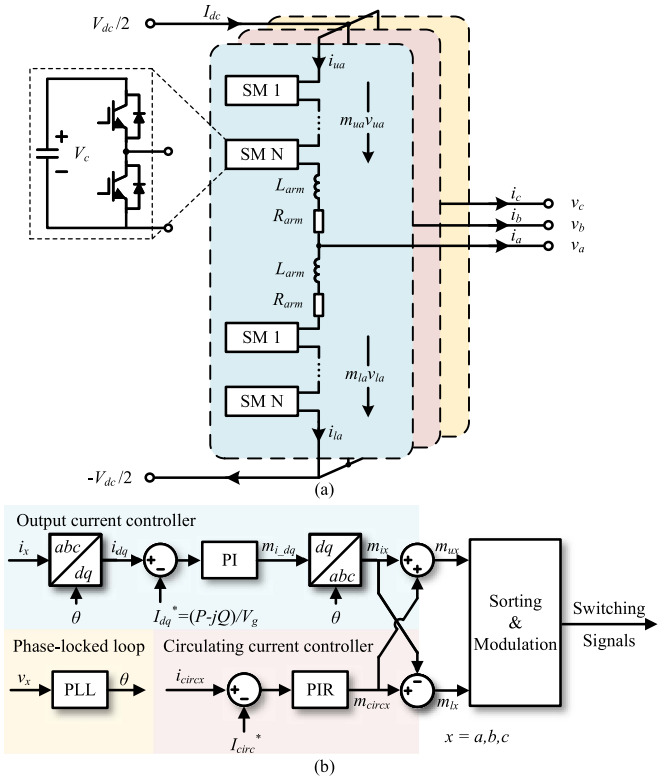

Fig. 1. Configuration of the studied MMC: (a) Electrical circuit and (b) control structure.

II. Sequence Impedance Model of the MMC

A. Unified Sequence Impedance Model of the MMC

A sequence impedance model is used to describe the ac-side impedance response of an MMC in Fig. 1 and investigate its small-signal stability. The detailed development of the MMC sequence impedance model is derived in [25], which is the basis of the impedance model derivation in this section. According to the phase and sequence relationships among the six arms, the impedance model of a three-phase converter can be simplified as a single-arm model. Thus, only the state variables in the phase a upper arm, that is the arm current i_{au}, the sum of arm capacitor voltages v_{au} and the insertion index m_{au}, are used to describe the converter impedance and the subscript "au" is omitted in the following derivation.

Considering the harmonic couplings in MMCs, vectors of $2n+1$ elements are used to represent the complex Fourier coefficients of the harmonics in state variables, where the harmonic orders are $[-nf_1,\ldots,-f_1,0,f_1,\ldots,nf_1]^T$. The frequency-domain small-signal model of the power stage in the MMC is

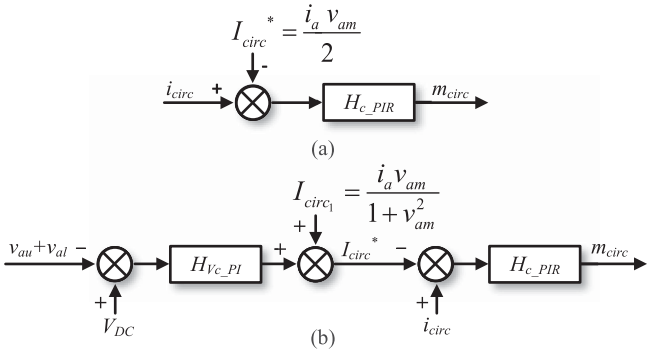

Fig. 2. Control diagram of circulating current injection methods based on instantaneous information: (a) Method 1 and (b) Method 2 [23].

converted from the time-domain switching average model, as

$$\begin{aligned}\hat{\mathbf{i}} &= -\mathbf{Y}_l\left(\hat{\mathbf{v}}_p + \mathbf{v}\otimes\hat{\mathbf{m}} + \mathbf{m}\otimes\hat{\mathbf{v}}\right)\\ \mathbf{Y}_c\hat{\mathbf{v}} &= \mathbf{i}\otimes\hat{\mathbf{m}} + \mathbf{m}\otimes\hat{\mathbf{i}}\end{aligned} \tag{1}$$

where $\hat{}$ variables are the Fourier coefficient vectors describing the small-signal harmonic components. $\hat{\mathbf{v}}_p$ is small-signal voltage perturbation of f_p injected at the ac-side terminals. The harmonic frequencies in the small-signal vectors are $[f_p - nf_1, \ldots, f_p - f_1, f_p, f_p + f_1, \ldots, f_p + nf_1]^T$. Harmonics up to the third-order ($n = 3$) are considered in the following analysis to reflect all critical impedance characteristics of an MMC system [24], [25], and the matrices in the model are 7×7 matrices. $\mathbf{Y}_l$ and $\mathbf{Y}_c$ are the diagonal admittance matrices of the arm inductance and the equivalent arm capacitance, respectively. The vector convolution in (1) can be converted into dot multiplication by introducing Toeplitz matrices of the steady-state harmonics for state variables, denoted as $\mathbf{M}$, $\mathbf{I}$, and $\mathbf{V}$.

The control stage model of the MMC reveals the dependence of the insertion indices on the other state variables as well as the injected voltage perturbation in Fig. 1(b), which can be expressed as

$$\hat{\mathbf{m}} = \mathbf{Q}\hat{\mathbf{i}} + \mathbf{E}\hat{\mathbf{v}} + \mathbf{P}\hat{\mathbf{v}}_p \tag{2}$$

The coefficient matrix $\mathbf{Q}$ is related to both output and circulating current controllers, while matrices $\mathbf{E}$ and $\mathbf{P}$ describe the capacitor voltage controller and phase-locked loop (PLL), respectively. In this article, a proportional-integral (PI) controller is adopted to regulate the output current in the dq frame. The circulating current control schemes are shown in Fig. 2 [23]. The circulating current reference is determined by instantaneous information, and a proportional-integral-resonant (PIR) controller in the abc frame is used to regulate both the dc component and second-order ac component.

By substituting (2) into (1), a $(2n+1)\times(2n+1)$ admittance matrix can be derived as

$$\begin{aligned}\mathbf{Y} = &\Big[\mathbf{U} + \mathbf{Y}_l\left(\mathbf{M}+\mathbf{VE}\right)\left(\mathbf{U}-\mathbf{Z}_c\mathbf{IE}\right)^{-1}\mathbf{Z}_c\mathbf{M}\\ &+ \mathbf{Y}_l\left(\mathbf{V}+\left(\mathbf{M}+\mathbf{VE}\right)\left(\mathbf{U}-\mathbf{Z}_c\mathbf{IE}\right)^{-1}\mathbf{Z}_c\mathbf{I}\right)\mathbf{Q}\Big]^{-1}\\ &\cdot \mathbf{Y}_l\left[\mathbf{U} + \left(\mathbf{V}+\left(\mathbf{M}+\mathbf{VE}\right)\left(\mathbf{U}-\mathbf{Z}_c\mathbf{IE}\right)^{-1}\mathbf{Z}_c\mathbf{I}\right)\mathbf{P}\right]\end{aligned} \tag{3}$$

where $\mathbf{U}$ is an identity matrix, and $\mathbf{Z}_c$ is the inverse matrix of $\mathbf{Y}_c$. The admittance matrix demonstrates the relationships between current and voltage harmonics at multiple frequencies. To analyze the stability of a grid-connected MMC, the coupling between positive and negative sequences is considered by the off-diagonal entries in the full ac-side admittance model, that is

$$\mathbf{Y}_{\text{MMC}} = \begin{bmatrix}\mathbf{Y}_{pp}(s) & \mathbf{Y}_{pn}\left(s-2j\omega_1\right)\\ \mathbf{Y}_{np}(s) & \mathbf{Y}_{nn}\left(s-2j\omega_1\right)\end{bmatrix}. \tag{4}$$

The admittance entries are extracted from (3), when a positive- or negative-sequence perturbation is injected [25].

B. Sequence Impedance Model of MMCs With Circulating Current Injection Methods

The MMC impedance is significantly influenced by the calculation of the circulating current reference. With the injection of second-harmonic circulating current, the capacitor voltage ripples in the MMC can be suppressed, and the calculation of the circulating current reference is facilitated by the methods proposed in [23]. The corresponding sequence impedance model is developed in [24]. When Method 1 [see Fig. 2(a)] is adopted, the circulating current reference is determined by the instantaneous output current i_a and normalized modulation voltage v_{am}. The coefficient matrices in (2) are modified as

$$\begin{aligned}\mathbf{Q} &= \mathbf{Q}_i + \mathbf{Q}_c\left(\mathbf{U} + 2\mathbf{M}_i\mathbf{T}_{\text{DM}} + \mathbf{I}_a\mathbf{Q}_i\right)\\ \mathbf{P} &= \left(\mathbf{U} + \mathbf{Q}_c\mathbf{I}_a\right)\mathbf{P}_{\text{PLL}}\\ \mathbf{E} &= \boldsymbol{O}_{2n+1,2n+1}.\end{aligned} \tag{5}$$

The matrices $\mathbf{Q}_i$, $\mathbf{Q}_c$, and $\mathbf{P}_{\text{PLL}}$ are the original matrices of the corresponding controller transfer functions. $\mathbf{M}_i$ and $\mathbf{I}_a$ are the Toeplitz matrices of the steady-state ac components in the insertion index and output current in phase a, respectively. $\mathbf{T}_{\text{DM}}$ is a diagonal matrix used to extract the DM components. The terms $\mathbf{Q}_c\mathbf{I}_a\mathbf{Q}_i$ and $\mathbf{Q}_c\mathbf{I}_a\mathbf{P}_{\text{PLL}}$ indicate the couplings between the circulating current controller, output current controller, and PLL controller, which are introduced by the circulating current reference calculation.

If Method 2 [see Fig. 2(b)] is used, a PI capacitor voltage controller, which is used to regulate the capacitor voltage of one phase leg, generates a CM compensation component in the circulating current reference. The ac component is determined by the instantaneous output current i_a and normalized modulation voltage v_{am}, and its small-signal expression is

$$\hat{i}_{\text{circ}_1}^{*} = \frac{V_{\text{am}}}{1+V_{\text{am}}^2}\hat{i}_a + \frac{I_a - 2I_{\text{circ}_1}^{*}V_{\text{am}}}{1+V_{\text{am}}^2}\hat{v}_{\text{am}}. \tag{6}$$

The capitalized variables are the steady-state values of the corresponding variables. The corresponding control stage model in (2) is

$$\begin{aligned}\mathbf{Q} &= \mathbf{Q}_i + \mathbf{Q}_c\left(\mathbf{U} - 2\left(\mathbf{C}_1\mathbf{T}_{\text{DM}} - \mathbf{C}_2\mathbf{Q}_i\right)\right)\\ \mathbf{P} &= \left(\mathbf{U} + 2\mathbf{Q}_c\mathbf{C}_2\right)\mathbf{P}_{\text{PLL}}\end{aligned}$$

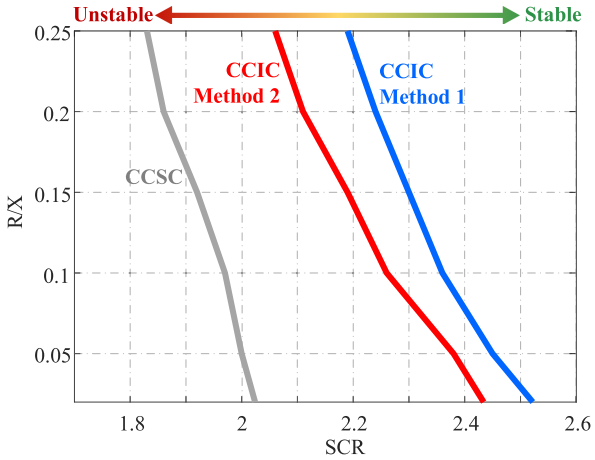

Fig. 3. Stability boundary comparison of different circulating current control schemes [24].

$$\mathbf{E} = 2\mathbf{Q}_c\mathbf{E}_c. \tag{7}$$

$\mathbf{C}_1$ and $\mathbf{C}_2$ are the Toeplitz matrices of the steady-state coefficients in (6). $\mathbf{E}_c$ is the transfer function matrix of the PI capacitor voltage controller. Compared with the control stage model of Method 1 in (5), an additional coupling between the circulating current controller and capacitor voltage controller is introduced by the term $\mathbf{Q}_c\mathbf{E}_c$.

C. Stability Limits of Circulating Current Injection Methods

Due to controller couplings, the sequence impedance of the MMC is influenced by the instantaneous circulating current reference, especially in the low frequency range, which is related to MMC internal dynamics [24]. The stability of the grid-connected MMC is consequently undermined by the low-frequency impedance shaping effects.

The stability impact of different circulating current references in MMCs is demonstrated by a stability boundary map in Fig. 3 with respect to system short-circuit-ratio (SCR) and resistance-reactance (R/X) ratio, which are indicators of grid strength. Identical circulating current regulators, i.e., PIR regulators with the same controller gains, are used to control both dc and second-harmonic components. For each stability boundary curve, if the grid operation point is on the right side of the boundary, the system will be stable under small-signal disturbances. Otherwise, the system is prone to instabilities. Compared with the conventional CCSC scheme where the circulating current reference is constantly zero, the system stability regions for Methods 1 and 2 are reduced by the controller couplings introduced by the reference calculation. Therefore, only CCSC can be adopted to guarantee system stability, when the grid strength decreases, which becomes a common scenario due to the increasing penetration of inverter based resources. As a result, the capacitor voltage ripples will increase and a larger submodule capacitor is required. To extend the stability regions of instantaneous circulating current injection methods, damping methods are critical to shape the MMC impedance and avoid interactions between the MMC and the grid, so that the submodule capacitor voltage ripples in MMCs can be optimized when they are connected to a weak grid.

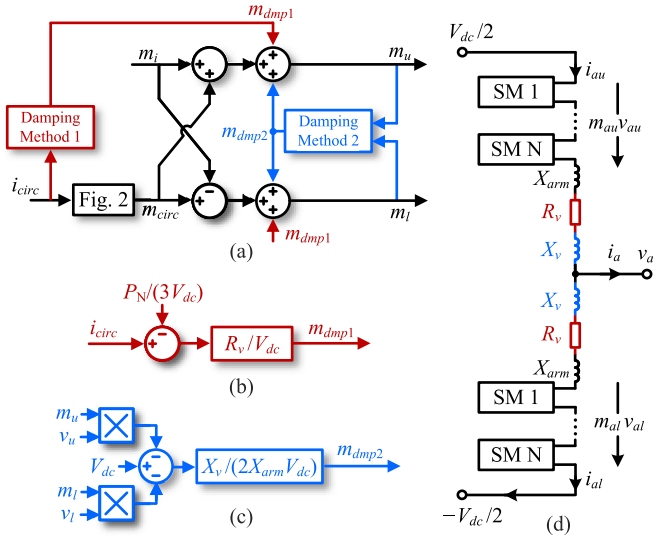

Fig. 4. Control diagram of active damping methods: (a) General control diagram; (b) Damping Method 1; (c) Damping Method 2; and (d) Equivalent virtual impedance.

III. Active Damping Schemes and Virtual Impedance in MMCs

Adding virtual impedance into the MMC can improve system stability without introducing extra components or increasing manufacturing cost [8], [10]. The control diagrams of the proposed active damping control schemes are presented in Fig. 4. A CM damping component $\hat{\mathbf{m}}_{\text{dmp}}$ is added in the insertion index to emulate virtual impedance in the converter arms. The equivalent small-signal model of the control stage is

$$\hat{\mathbf{m}} = \mathbf{Q}\hat{\mathbf{i}} + \mathbf{E}\hat{\mathbf{v}} + \mathbf{P}\hat{\mathbf{v}}_p + \hat{\mathbf{m}}_{\text{dmp}}. \tag{8}$$

The virtual impedance is generated by the injected second-harmonic circulating current, which consists of virtual resistance, reactance, or both.

A. Virtual Resistance R_v

A virtual arm resistor is emulated at second-harmonic frequency, as shown in Fig. 4(b). In order to maintain the power balance between dc and ac sides, the dc component estimated by the output power P_N is subtracted from the circulating current. The normalized voltage drop across the virtual resistance R_v, which is generated by the injected second-harmonic circulating current, is added to the modulation signal. The expression of the damping insertion index is

$$m_{\text{dmp1}} = \frac{R_v}{V_{\text{dc}}}\left(i_{\text{circ}} - \frac{P_N}{3V_{\text{dc}}}\right) \tag{9}$$

and the small-signal model in the frequency domain is

$$\hat{\mathbf{m}}_{\text{dmp1}} = \frac{R_v}{V_{\text{dc}}}\hat{\mathbf{i}}_{\text{circ}} = \frac{R_v}{V_{\text{dc}}}\mathbf{T}_{\text{cm}}\hat{\mathbf{i}}. \tag{10}$$

TABLE I
PARAMETERS OF THE MMC MODEL

Parameter		Simulation value	Experimental value
Rated power		800 MW	1 kW
DC bus voltage		±200 kV	200 V
AC voltage		220 kV (L-L rms)	70 V
SMs per arm		200	8
SM capacitance		10 mF	5.93 mF
Arm inductance		29 mH	6 mH
Output current controller (PI)	K_p	0.24	3
	K_i	74.5	800
Circulating current controller (PR)	K_p	0.5	2
	K_r	60	600
PLL (SRF)	K_p	300	1.88
	K_i	200	1500

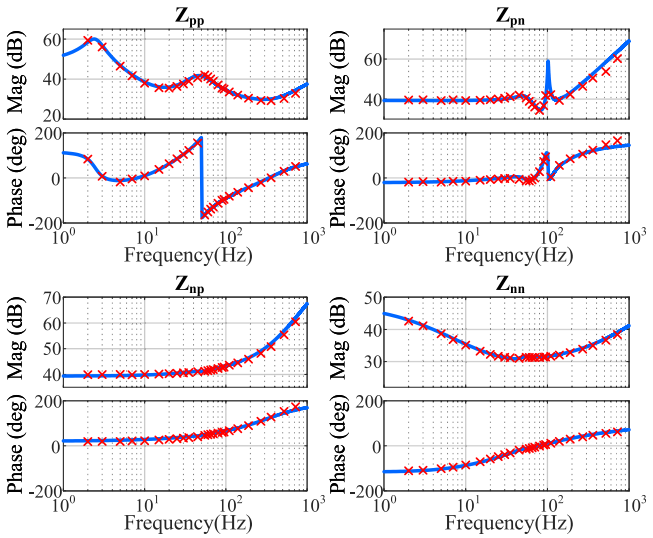

Fig. 5. Impedance model of MMC with virtual arm resistance $R_v = 36\,\Omega$ (blue lines: analytical impedance; red crosses: frequency scanning results).

$\mathbf{T}_{\text{cm}}$ is the matrix used to extract the CM circulating current in the arm current.

The MMC equivalent circuit of phase a is presented in Fig. 4(d), where virtual resistors R_v are added in both upper and lower arms. To evaluate the system stability, the control stage model is modified by substituting (8) and (10) into (2)

$$\begin{aligned}\mathbf{Q}_1 &= \mathbf{Q} + \frac{R_v}{V_{\text{dc}}}\mathbf{T}_{\text{cm}}\\ \mathbf{P}_1 &= \mathbf{P}\\ \mathbf{E}_1 &= \mathbf{E}.\end{aligned} \tag{11}$$

The proposed damping method is validated based on the MMC simulation model in [26], with circulating current injection Method 1. The detailed parameters of the simulation system are listed in Table I. The sequence impedance model of the MMC with a virtual resistor of 36 Ω (0.6 p·u·) is presented in Fig. 5. The selection of damping parameter will be explored later in this article. In Fig. 5, the frequency scanning results match well with the analytical results in terms of all elements in

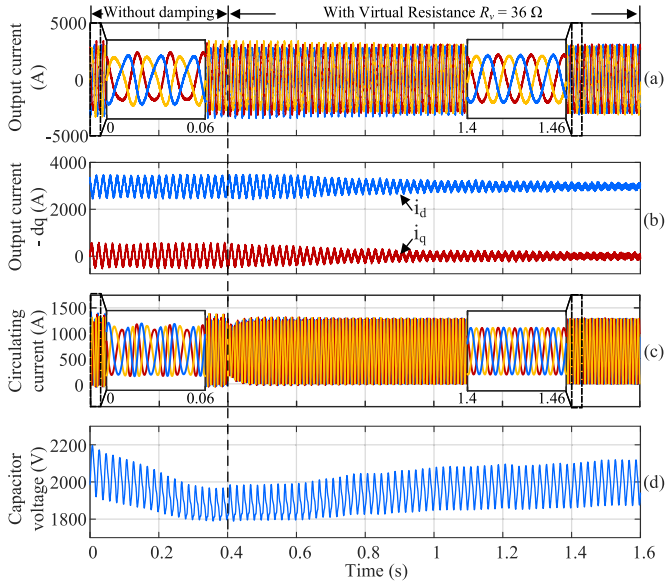

Fig. 6. Grid interaction study of the MMC with virtual arm resistance $R_v = 36\,\Omega$ (SCR = 2.37): (a) *Abc*-frame output current, (b) *dq*-frame output current, (c) circulating current, and (d) capacitor voltage.

the sequence impedance model. With virtual arm resistance, the MMC impedance is reshaped in the low frequency range, i.e., the frequency below 20 Hz, which is well-suited for addressing subsynchronous oscillations caused by circulating current controllers. As shown in Fig. 6, the oscillations of the MMC are stabilized by introducing the virtual resistance at $t = 0.4$ s, when the MMC is connected to a weak grid with an SCR of 2.37. The steady-state values of the circulating current and capacitor voltage, which are related to the MMC internal dynamics, still remain at their references with the virtual resistance.

B. Virtual Reactance X_v

With second-order harmonics in the circulating current, adding a virtual reactance in the arm can also improve system stability. Similar with the realization of virtual resistance, the normalized voltage across the virtual reactance is added in the insertion index. The damping component can be expressed as

$$m_{\text{dmp}} = \frac{L_v}{V_{\text{dc}}}\frac{di_{\text{circ}}}{dt} \tag{12}$$

where the derivative of the circulating current is calculated. However, a derivative controller is not realizable in a practical control loop. The limited sampling frequency in the MMC can introduce significant noise in the output of the damping controller and consequently undermines the system stability.

To avoid the noise introduced by the derivative controller, the voltage across the existing arm reactor can be instead used for emulating the virtual reactance. First, the voltage across the upper-arm and lower-arm impedance in one phase is calculated by subtracting the arm capacitor voltage from the bus voltage:

$$v_{X\text{arm}} = V_{\text{dc}} - (m_u v_u + m_l v_l) \tag{13}$$

where the resistance of the arm reactor is neglected.

In the sum of the upper- and lower-arm capacitor voltages, only the CM components are taken into consideration and the DM components are canceled out. As shown in Fig. 4(c), the normalized voltage across the virtual reactance X_v for one arm can be derived as

$$m_{\text{dmp2}} = \frac{X_v}{2X_{\text{arm}}V_{\text{dc}}}\left[V_{\text{dc}} - (m_u v_u + m_l v_l)\right] \tag{14}$$

given that the virtual reactances in the upper and lower arms are equal. The equivalent circuit with the virtual reactance is presented in Fig. 4(c). The frequency-domain small-signal model of the damping method is

$$\begin{aligned}\hat{\mathbf{m}}_{\text{dmp2}} &= -\frac{X_v}{2X_{\text{arm}}V_{\text{dc}}} \\ &\quad \cdot (\mathbf{m}_u \otimes \hat{\mathbf{v}}_u + \mathbf{v}_u \otimes \hat{\mathbf{m}}_u + \mathbf{m}_l \otimes \hat{\mathbf{v}}_l + \mathbf{v}_l \otimes \hat{\mathbf{m}}_l) \\ &= -\frac{X_v}{X_{\text{arm}}V_{\text{dc}}}\mathbf{T}_{\text{CM}}\left(\mathbf{M}\hat{\mathbf{v}} + \mathbf{V}\hat{\mathbf{m}}\right)\end{aligned} \tag{15}$$

where $\mathbf{m}_u$, $\mathbf{v}_u$, $\mathbf{m}_l$, and $\mathbf{v}_l$ are the steady-state harmonic vectors of insertion index and capacitor voltage in upper and lower arms, respectively. The $\hat{}$variables are the corresponding small-signal harmonic vectors. $\mathbf{T}_{CM}$ extracts the CM components and cancels the DM components in the state variables.

The complete control stage model of the MMC is updated by substituting (8) and (15) into (1)

$$\begin{aligned}\mathbf{Q}_2 &= \left(\mathbf{U} + \frac{X_v}{X_{\text{arm}}V_{\text{dc}}}\mathbf{T}_{\text{cm}}\mathbf{V}\right)^{-1}\mathbf{Q} \\ \mathbf{P}_2 &= \left(\mathbf{U} + \frac{X_v}{X_{\text{arm}}V_{\text{dc}}}\mathbf{T}_{\text{cm}}\mathbf{V}\right)^{-1}\mathbf{P} \\ \mathbf{E}_2 &= \left(\mathbf{U} + \frac{X_v}{X_{\text{arm}}V_{\text{dc}}}\mathbf{T}_{\text{cm}}\mathbf{V}\right)^{-1}\left(\mathbf{E} - \frac{X_v}{X_{\text{arm}}V_{\text{dc}}}\mathbf{T}_{\text{cm}}\mathbf{M}\right).\end{aligned} \tag{16}$$

The sequence impedance model of the MMC with virtual arm inductance is presented in Fig. 7. The added virtual reactance is 36 Ω (0.6 p·u·) at second-harmonic frequency, double of the existing arm inductor. The frequency scanning results match well with the analytical impedance over the entire frequency range, verifying the accuracy of the impedance model. The damping effect of the proposed virtual reactance is validated in Fig. 8. The MMC system is initially unstable with the SCR of 2.37, and the virtual reactance is added at $t = 0.4$ s to stabilize the system. With the virtual reactance, the oscillations are suppressed after a transient of 0.4 s (at $t = 0.8$ s).

When both virtual resistance and inductance are added in the MMC, the CM damping component $\hat{\mathbf{m}}_{\text{dmp}}$ in (8) is the sum of $\hat{\mathbf{m}}_{\text{dmp1}}$ and $\hat{\mathbf{m}}_{\text{dmp2}}$ in (10) and (15), respectively. With the combination of virtual resistance and reactance, the magnitude and phase of the virtual impedance can be controlled flexibly so that the effectiveness of the active damping method is optimized under specific grid conditions.

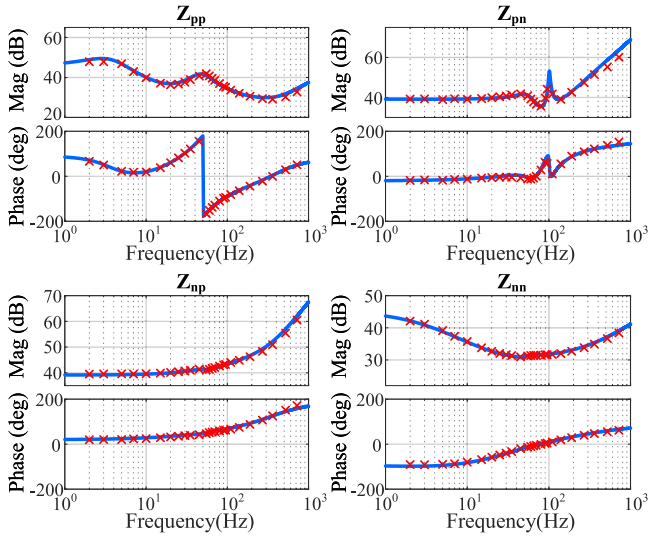

Fig. 7. Impedance model of MMC with virtual arm reactance $X_v = 36\ \Omega$ (blue lines: analytical impedance; red crosses: frequency scanning results).

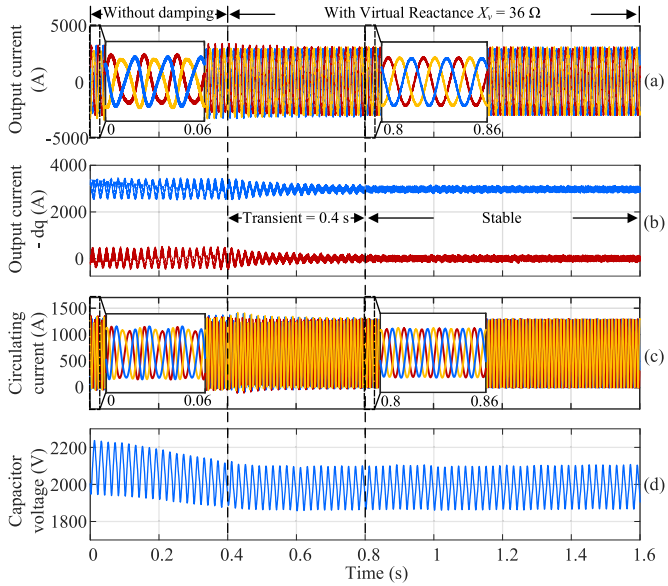

Fig. 8. Grid interaction study of the MMC with virtual arm reactance $X_v = 36\ \Omega$ (SCR = 2.37): (a) Abc-frame output current, (b) dq-frame output current, (c) circulating current, and (d) capacitor voltage.

IV. Real-Time Validation and Comparison of Virtual Impedance

To validate and compare the proposed damping methods, a high-voltage real-time MMC system is developed (see Table I). The real-time simulation is implemented in one RTDS rack with 5 PB5 processor boards. The small time-step for the MMC power stage is 2 μs, and the simulation time-step for the control stage is 30 μs.

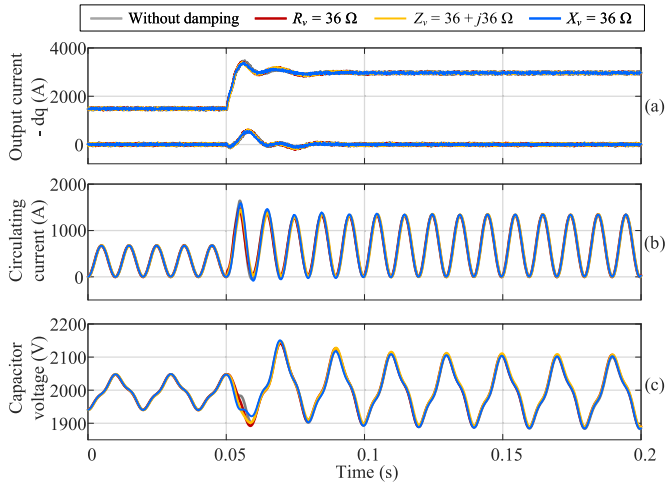

Fig. 9. MMC performance under a power step from 400 to 800 MW when it is connected to a strong grid (SCR = 4.5): (a) dq-frame output current, (b) circulating current, and (c) capacitor voltage.

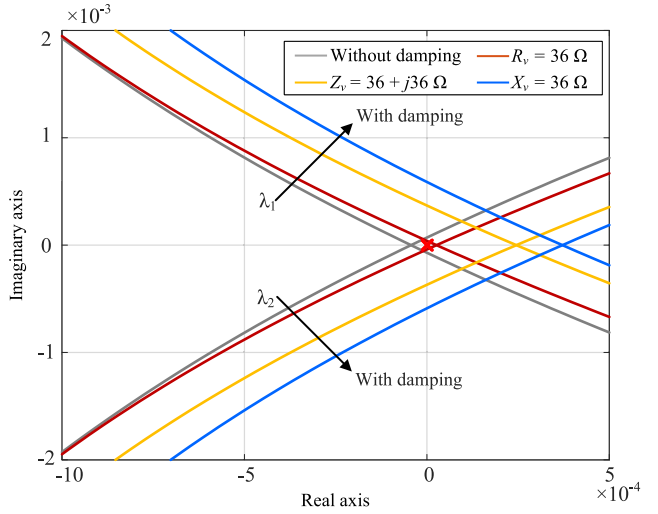

Fig. 10. Eigenloci of the return ratio matrix with different damping methods when the MMC is connected to a weak grid (SCR = 2.37).

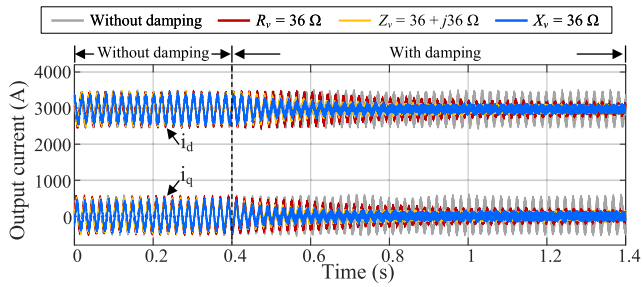

Fig. 11. Comparison of the output current in dq frame with different damping methods when the MMC is connected to a weak grid (SCR = 2.37).

A. Comparison of Active Damping Methods

Three different cases are developed to compare the damping effects of the proposed methods, i) pure virtual resistance R_v, ii) pure virtual reactance X_v and iii) combined virtual impedance $(R_v + X_v)$. The virtual reactance X_v has the same impedance value with the virtual resistance R_v at second-harmonic frequency.

The MMC performance with different damping methods, when it is connected to a strong grid with the system SCR of 4.5 [27] are first compared. A power step from 400 to 800 MW is applied at $t = 0.05$ s. As shown in Fig. 9, all active damping methods have similar steady-state performances compared with the original case (without damping), in terms of output current, circulating current, and capacitor voltage. Therefore, the damping methods can be adopted during normal operations regardless of grid conditions. The virtual impedance is emulated by adding a damping component, which is generated by the injected second-harmonic circulating current, instead of the dc component. Therefore, the power is balanced between the dc and ac sides, so that the submodule capacitor voltage can be maintained at its reference.

The damping effect of the proposed methods is also evaluated by both theoretical analysis and simulation results. The system stability is first analyzed based on the impedance return ratio matrix, considering the couplings between the positive and negative sequences [28]. The eigenloci (λ_1 and λ_2) of the return ratio matrix are presented in Fig. 10 when the MMC is connected to a weak grid with an SCR of 2.37. The eigenloci encircle $(-1, j0)$ when the damping methods are not adopted, which indicates the grid-connected MMC is unstable according to the Generalized Nyquist Criterion (GNC) [29]. As shown in Fig. 11, there is an undamped oscillation of 49 Hz in the dq-frame output current of the MMC without damping methods. After a virtual impedance is added at $t = 0.4$ s, the intersections between the eigenloci and the real axis move rightward, and the eigenloci stop encircling $(-1, j0)$. The stability margin of the interconnected system increases, and the oscillation stops gradually in Fig. 11. The settling time of the MMC with virtual resistance is the longest of all three cases, corresponding to the lowest stability margin in Fig. 10. As for the virtual reactance and combined impedance, the stability margin is similar, with shorter settling time than the virtual resistance for both cases. Therefore, in the combined impedance, the damping effect of the virtual reactance is more significant. In the following analysis, the virtual reactance is adopted for better stability improvement.

Both arm impedance emulation methods can be combined with the ac virtual resistance emulation method, which is emulated by introducing a feedforward proportional component of the output current to the DM insertion indices [18]. The proposed virtual arm impedance and the conventional virtual ac resistance emulations are decoupled and can be implemented independently to achieve a better active damping effect.

B. Selection of Damping Parameters

The damping effect of different virtual reactances is investigated in Fig. 12, to explore the optimal parameters. The added reactance value is from 18 Ω to 72 Ω at the second-harmonic frequency, corresponding to one to four times of the original arm reactance (0.3 p·u· to 1.2 p·u·). The MMC is connected to a

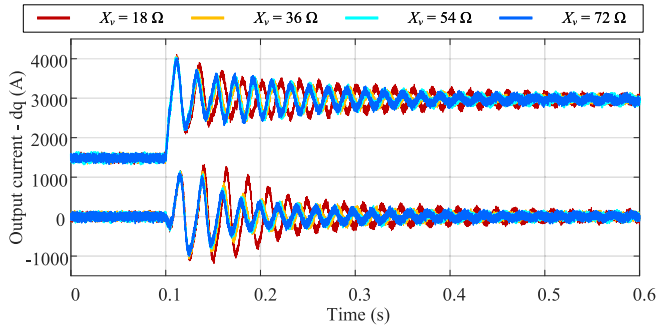

Fig. 12. Comparison of the output current in dq frame with different virtual reactances when SCR = 2.25.

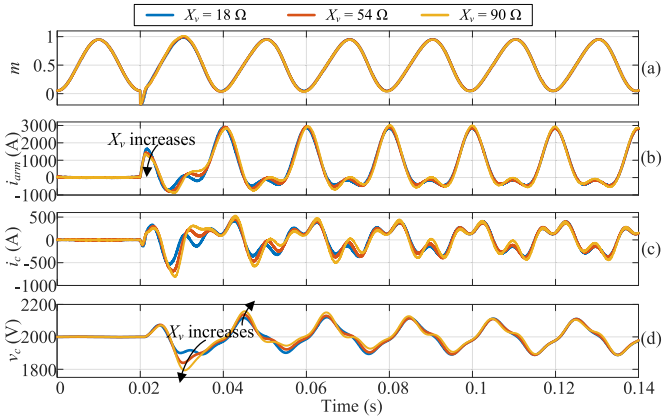

Fig. 13. MMC dynamic performance with different virtual reactance when a power step from 0 to 800 MW is applied at $t = 0.02$ s.

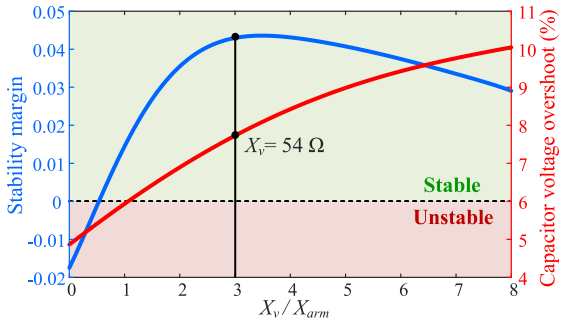

Fig. 14. System stability margin and capacitor voltage overshoot with different virtual reactance when SCR = 2.25.

weak grid with the SCR of 2.25, and the interconnected system is stable for all cases when the MMC output power is 400 MW. At $t = 0.1$ s, a power step to 800 MW is applied, and the oscillations are suppressed by the introduction of virtual reactance. The current peak value in the first period after the power step is similar for all cases, but the settling time is improved with the increase of virtual reactance, corresponding to the enhanced stability margin.

The system stability margin is quantified by the distance from $(-1, j0)$ to the intersection between the return ratio matrix eigenloci and the negative real axis. As shown in Fig. 14, the

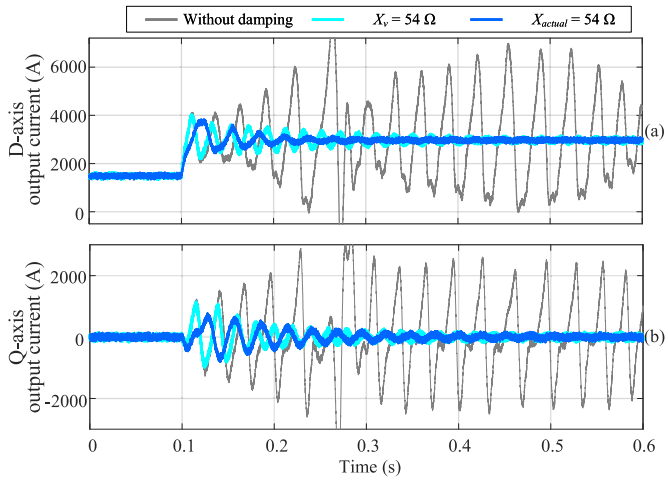

Fig. 15. Damping effect comparison of actual and virtual reactance when SCR = 2.25.

grid-connected MMC is stable when the system stability margin is positive. The system stability margin is maximized when the virtual reactance is three to four times of the original arm reactance, for the specific simulation model and grid condition. However, the increase of virtual reactance will compromise the dynamic performance of the MMC. For example, the maximum capacitor voltage overshoot increases monotonically in Fig. 13, when a power step from 0 to 800 MW is applied at $t = 0.02$ s. The capacitor current, which is the product of the insertion index and arm current, has larger oscillations and longer settling time after the power step, which consequently leads to a higher capacitor voltage overshoot. The overshoot of the capacitor voltage is affected by the specific operation condition including the power step time and step magnitude. Considering both system stability and MMC internal dynamics in Fig. 14, a virtual reactance of 54 Ω (0.9 pu) is adopted in the following case studies.

The comparison of passive and active damping methods is demonstrated in Fig. 15. The MMC without damping method fails to maintain stability after the power increases from 400 to 800 MW at $t = 0.1$ s. Actual and virtual reactors of the same value (54 Ω) are added to suppress the oscillation, respectively. The passive method mitigates the oscillation with slightly faster speed, compared with the virtual reactance of the same value. However, the excessively large arm reactor will undermine the dynamic response as well as the dc voltage utilization of the MMC. On the other hand, the active damping method can be tuned flexibly by modifying the controller gains according to the specific grid conditions.

C. Small-Signal Stability Improvement

The MMC stability boundary map, presented in Fig. 16, is used to quantify the stability improvement of the proposed active damping methods. According to Fig. 3 [24], when instantaneous circulating current injection methods are adopted, the stability region of the grid-connected MMC is reduced due to the controller couplings in the circulating current reference calculation process. With a virtual reactance of 54 Ω, the original

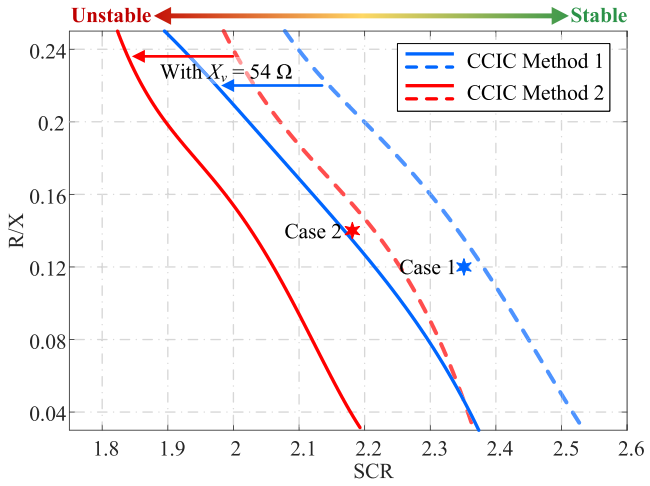

Fig. 16. Improvement of the MMC stability boundaries with $X_v = 54\ \Omega$.

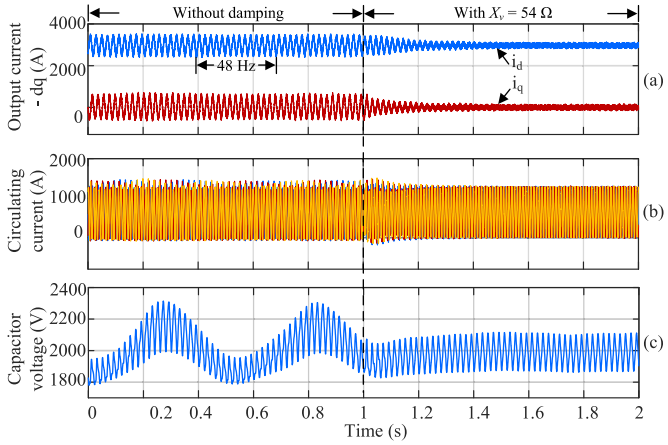

Fig. 17. Case 1: Validation of the proposed damping method when instantaneous circulating current Method 1 is used under the unity power factor: (a) dq-frame output current, (b) circulating current, and (c) capacitor voltage.

MMC stability boundaries (the dash lines in Fig. 16) are moved leftward, referring to the extension of stability regions.

The proposed damping methods are feasible when either Method 1 or Method 2 in Fig. 2 is used, as the references for both circulating current injection methods are determined by the instantaneous information adaptively. The stability boundaries are validated by two grid interaction studies, which are annotated in Fig. 16. The case study results are presented in Figs. 17 and 18. When the virtual impedance is added at $t = 1$ s, the unstable system is stabilized. After reaching steady state, the harmonics in the output current, circulating current, and capacitor voltage are not affected by the proposed damping method. The proposed method can also be used when the MMC provides/absorbs active and reactive power to the grid. A case study is provided in Fig. 19. The MMC power setting point is 600 MW, -320 MVar. The system is initially unstable without the virtual arm impedance, and an undamped oscillation is observed in the dq-frame current. At $t = 1$ s, a virtual arm reactance of 54

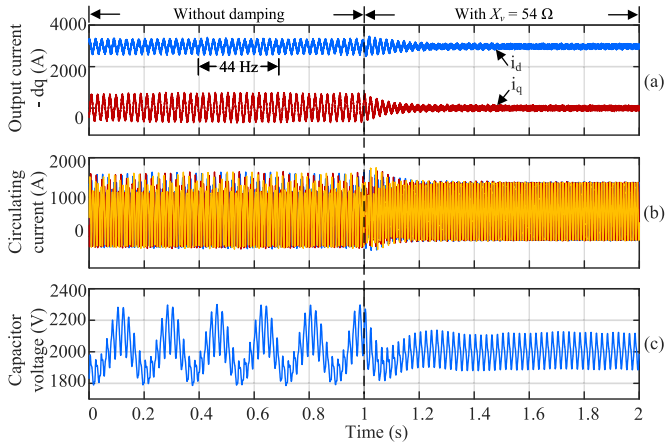

Fig. 18. Case 2: Validation of the proposed damping method when instantaneous circulating current Method 2 is used under the unity power factor: (a) dq-frame output current, (b) circulating current, and (c) capacitor voltage.

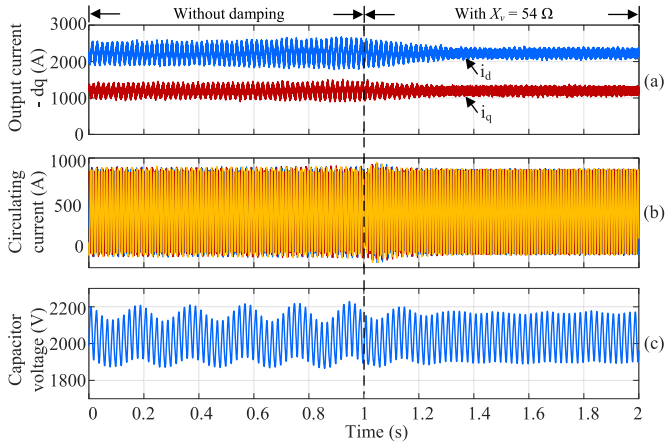

Fig. 19. Case 3: Validation of the proposed damping method when instantaneous circulating current Method 1 is used under the nonunity power factor: (a) dq-frame output current, (b) circulating current, and (c) capacitor voltage.

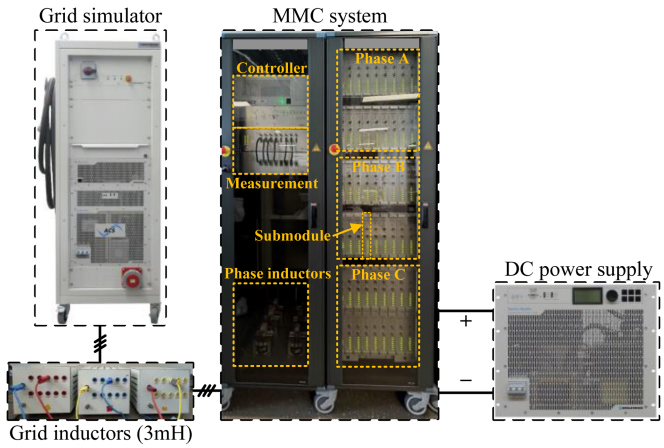

Fig. 20. Configuration and parameters of the grid-connected MMC experimental prototype. The experimental setup is operated below its rated capability to minimize issues during oscillations.

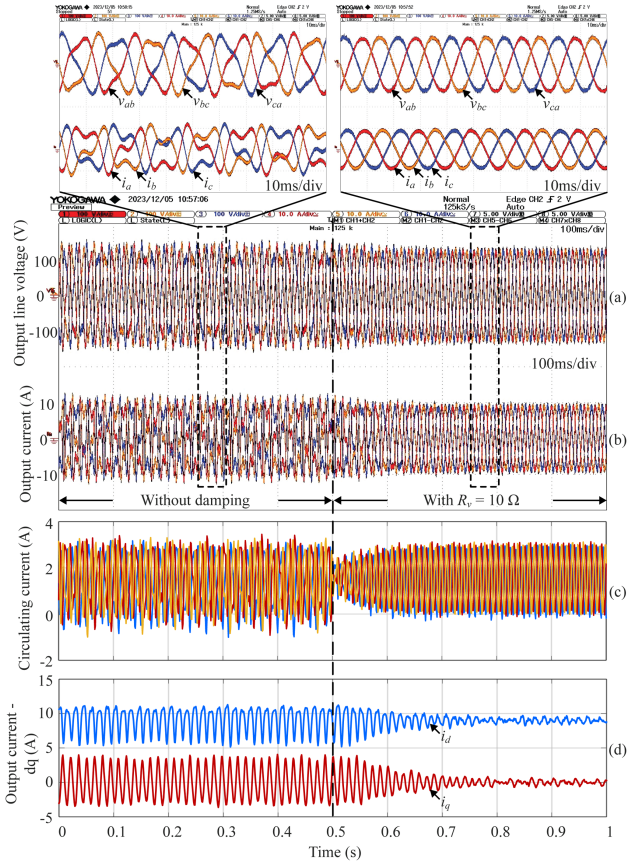

Fig. 21. Experimental validation of virtual arm resistance R_v. A virtual arm resistance of 10 Ω is applied at $t = 1$ s to suppress oscillations: (a) Output line voltage, (b) output current, (c) circulating current, and (d) dq-frame output current.

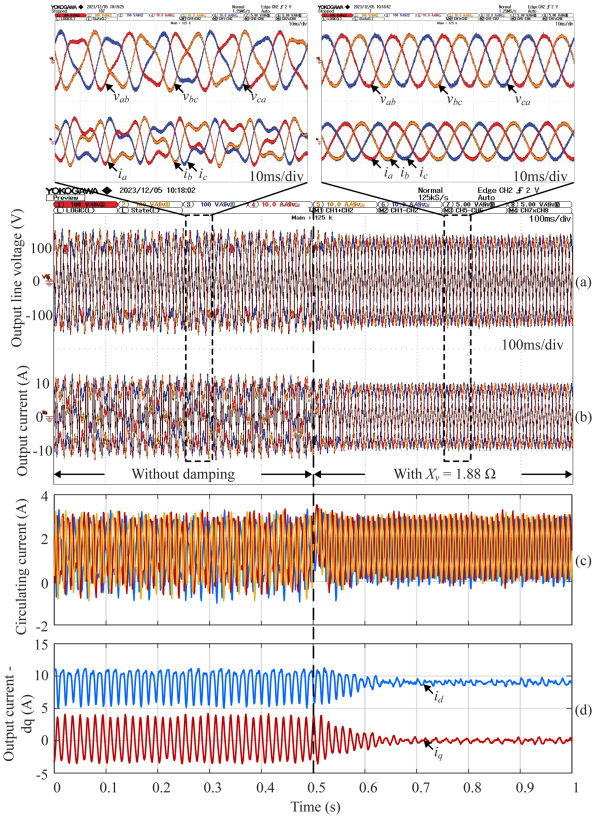

Fig. 23. Experimental validation of virtual arm reactance X_v. A virtual arm reactance of 1.88 Ω is applied at $t = 1$ s to suppress oscillations: (a) Output line voltage, (b) output current, (c) circulating current, and (d) dq-frame output current.

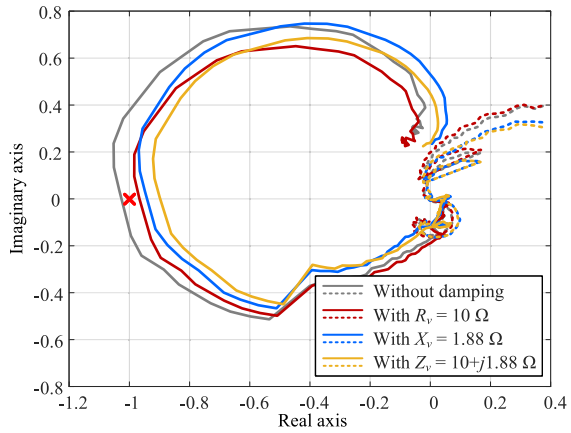

Fig. 22. Eigenloci of $Z_g Y_{\text{MMC}}$ in the experiments: The critical point $(-1, j0)$ is not encircled when virtual arm impedance is added (1–150 Hz).

Ω is added. The oscillation is suppressed by the virtual arm reactance, validating the effectiveness of the proposed method nonunity power factor operation.

V. Experimental Validation of Virtual Arm Impedance

The small-signal stability enhancement of the virtual arm impedance is validated on a grid-connected MMC in Fig. 20 [30], of which the system parameters are shown in Table I. The MMC is equipped with eight submodules in each arm. The dc power is provided by a REGATRON TopCon Quadro power supply, and the ac terminals of the MMC are connected to a REGATRON TC.ACS grid simulator using grid inductors of 3 mH.

Fig. 21 presents the grid interaction of the MMC with virtual arm resistance. The line-to-line voltage and phase current in Fig. 21(a) and (b) are measured by probes and captured in an oscilloscope, while the circulating current and dq-frame current in Fig. 21(c) and (d) are calculated and recorded in dSPACE's runtime environment. The MMC is initially unstable without active damping methods when the output current is 9 A. Oscillations are observed in line voltage, output current, and circulating current. The instability is aligned with the theoretical stability analysis in Fig. 22. The theoretical admittance of the experimental setup Y_{MMC} is obtained by frequency scanning in simulation, and the eigenloci of return ratio matrix $(Z_g Y_{\text{MMC}})$ are calculated for stability analysis. Without damping methods, the eigenloci encircle $(-1, j0)$. At $t = 1$ s, a virtual arm resistance

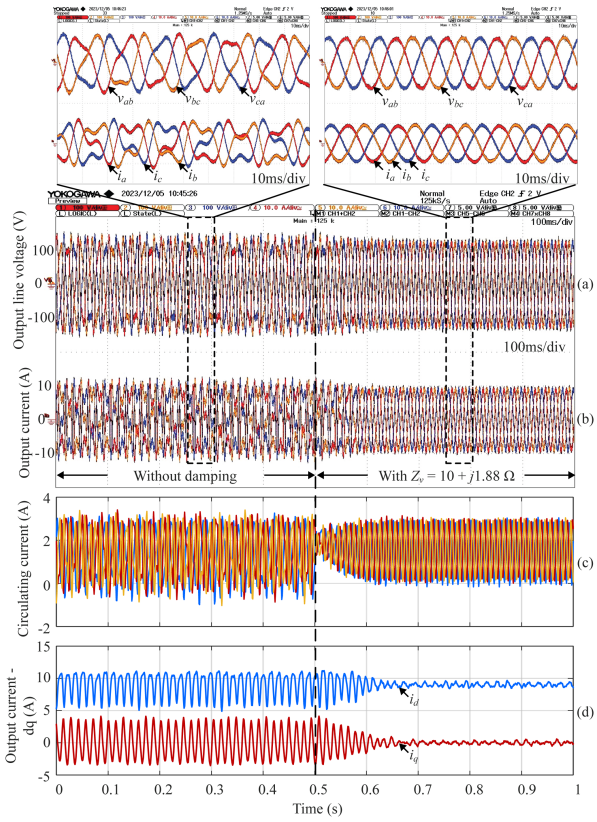

Fig. 24. Experimental validation of virtual arm impedance $R_v + jX_v$. A virtual arm reactance of $10 + j1.88\,\Omega$ is applied at $t = 1$ s to suppress oscillations: (a) Output line voltage, (b) output current, (c) circulating current, and (d) dq-frame output current.

of 10 Ω is added. The dynamic performance of the MMC matches with the real-time simulation in Fig. 6. The oscillations in the MMC are mitigated after 0.5 s, validating that the system eigenloci stop encircling $(-1, j0)$ in Fig. 22. With the virtual arm resistance, the steady-state performance of the MMC, including both output power and the internal dynamics, stays intact.

A virtual reactance of 1.88 Ω is added to suppress the oscillations in Fig. 23. The initial operation scenario is the same as the case study in Fig. 21, where the system is unstable with the oscillation of 66 Hz in the dq-frame output current. At $t = 1$ s, the virtual resistance is added, which suppress the oscillations within 0.2 s. The shorter settling time of the virtual reactance indicates the enhanced stability margin, compared with the virtual resistance of 10 Ω in Fig. 21. The comparison of the eigenloci in Fig. 22 also demonstrates that the virtual reactance has a better damping effect than virtual resistance under the experimental condition, because the eigenlocus of the MMC with virtual resistance is closer to $(-1, j0)$.

The combination of virtual reactance and resistance can also enhance the stability margin in the experimental setup. As shown in Fig. 24, a virtual impedance of $10 + j1.88\,\Omega$ is applied at $t = 1$ s to suppress the small-signal oscillations, which is validated by the theoretical stability margin in Fig. 22. Compared with the results in Fig. 23, the dynamic performance of circulating current in the MMC is improved by the virtual resistance, where the circulating current overshoot is dampened after adding the virtual arm impedance at $t = 1$ s.

VI. Conclusion

Active damping control schemes for MMCs have been proposed in this article to introduce virtual arm resistance and reactance by adding CM compensation terms in the insertion index, in order to improve system stability when instantaneous circulating current methods are used. The added damping component is the normalized voltage drop across the virtual impedance, which is determined by the internal variables and is unique in MMCs. The system stability margin is enhanced without compromising either internal or external steady-state performance. According to the theoretical analysis and real-time simulation results, introducing a virtual reactance can achieve better damping effect, compared with a virtual resistor of the same impedance. With the proposed active damping methods, the instantaneous circulating current injection methods can be adopted to reduce capacitor voltage ripples when the MMC is connected to a weaker grid.

References

[1] S. Debnath, J. C. Qin, B. Bahrani, M. Saeedifard, and P. Barbosa, "Operation, control, and applications of the modular multilevel converter: A review," *IEEE Trans. Power Electron.*, vol. 30, no. 1, pp. 37–53, Jan. 2015.

[2] M. A. Perez, S. Ceballos, G. Konstantinou, J. Pou, and R. P. Aguilera, "Modular multilevel converters: Recent achievements and challenges," *IEEE Open J. Ind. Electron. Soc.*, vol. 2, pp. 224–239, Feb. 2021.

[3] J. Lyu, X. Cai, and M. Molinas, "Optimal design of controller parameters for improving the stability of MMC-HVDC for wind farm integration," *IEEE J. Emerg. Sel. Topics Power Electron.*, vol. 6, no. 1, pp. 40–53, Mar. 2018.

[4] P. De Rua and J. Beerten, "Generalization of harmonic state-space framework to delayed periodic systems for stability analysis of the modular multilevel converter," *IEEE Trans. Power Del.*, vol. 37, no. 4, pp. 2661–2672, Aug. 2023.

[5] Y. Li, T. An, D. Zhang, X. Pei, K. Ji, and G. Tang, "Analysis and suppression control of high frequency resonance for MMC-HVDC system," *IEEE Trans. Power Del.*, vol. 36, no. 6, pp. 3867–3881, Dec. 2021.

[6] J. Freytes et al., "Improving small-signal stability of an MMC with CCSC by control of the internally stored energy," *IEEE Trans. Power Del.*, vol. 33, no. 1, pp. 429–439, Feb. 2018.

[7] B. Jacobson, P. Karlsson, G. Asplund, and T. J. Lennart Harnefors, "VSC-HVDC transmission with cascaded two-level converters," in *Proc. CIGRE*, Paris, France, 2010, pp. B4–110.

[8] B. Li, Z. Xu, S. Shi, D. Xu, and W. Wang, "Comparative study of the active and passive circulating current suppression methods for modular multilevel converters," *IEEE Trans. Power Electron.*, vol. 33, no. 3, pp. 1878–1883, Mar. 2018.

[9] Y. Li, E. A. Jones, and F. Wang, "Circulating current suppressing control's impact on arm inductance selection for modular multilevel converter," *IEEE J. Emerg. Sel. Topics Power Electron.*, vol. 5, no. 1, pp. 182–188, Mar. 2017.

[10] K. Ji, H. Pang, Z. He, Y. Li, D. Liu, and G. Tang, "Active/Passive method-based hybrid high-frequency damping design for MMCs," *IEEE J. Emerg. Sel. Topics Power Electron.*, vol. 9, no. 5, pp. 6086–6098, Oct. 2021.

[11] M. Nahalparvari, M. Asoodar, L. Bessegato, S. Norrga, and H.-P. Nee, "Modeling and shaping of the DC-side admittance of a modular multilevel converter under closed-loop voltage control," *IEEE Trans. Power Electron.*, vol. 36, no. 6, pp. 7294–7306, Jun. 2021.

[12] T. Huang, F. Yang, D. Zhang, and X. Chen, "High-frequency stability analysis and impedance optimization for an MMC-HVDC integrated system considering delay effects," *IEEE Trans. Emerg. Sel. Topics Circuits Syst.*, vol. 12, no. 1, pp. 59–72, Mar. 2022.

[13] J. Man, L. Chen, V. Terzija, and X. Xie, "Mitigating high-frequency resonance in MMC-HVDC systems ssing adaptive notch filters," *IEEE Trans. Power Syst.*, vol. 37, no. 3, pp. 2086–2096, May 2022.

[14] H. Wu, X. Wang, and L. H. Kocewiak, "Impedance-based stability analysis of voltage-controlled MMCs feeding linear AC systems," *IEEE J. Emerg. Sel. Topics Power Electron.*, vol. 8, no. 4, pp. 4060–4074, Dec. 2020.
[15] Y. Zhang, Y. Wang, D. Zhang, X. Chen, and C. Gong, "Broadband impedance shaping control scheme of MMC-based STATCOM for improving the stability of the wind farm," *IEEE Trans. Power Electron.*, vol. 36, no. 9, pp. 10278–10292, Sep. 2021.
[16] Y. Li et al., "Modeling and damping control of modular multilevel converter based DC grid," *IEEE Trans. Power Syst.*, vol. 33, no. 1, pp. 723–735, Jan. 2018.
[17] P. Li et al., "DC impedance modeling and design-oriented harmonic stability analysis of MMC-PCCF-based HVDC system," *IEEE Trans. Power Electron.*, vol. 37, no. 4, pp. 4301–4319, Apr. 2022.
[18] K. Ji et al., "Generalized impedance analysis and new sight at damping controls for wind farm connected MMC–HVdc," *IEEE J. Emerg. Sel. Topics Power Electron.*, vol. 9, no. 6, pp. 7278–7295, Dec. 2021.
[19] T. Liu, X. Wang, F. Liu, K. Xin, and Y. Liu, "A current limiting method for single-loop voltage-magnitude controlled grid-forming converters during symmetrical faults," *IEEE Trans. Power Electron.*, vol. 37, no. 4, pp. 4751–4763, Apr. 2022.
[20] X. Xiong, Y. Yang, C. Wu, C. Zhao, and F. Blaabjerg, "Improving the stability of standalone MMCs by shaping the AC side impedance using insertion index compensation," *IEEE Trans. Emerg. Sel. Topics Circuits Syst.*, vol. 12, no. 1, pp. 81–89, Mar. 2022.
[21] Z. Liu and J. Zhao, "Disturbance interaction analysis and suppression strategy of MMC-HVDC systems considering sub-module capacitor voltage ripples," *IEEE Trans. Power Syst.*, vol. 36, no. 1, pp. 235–247, Jan. 2021.
[22] J. Lyu, X. Cai, M. Amin, and M. Molinas, "Sub-synchronous oscillation mechanism and its suppression in MMC-based HVDC connected wind farms," *IET Gener. Transm. Distrib.*, vol. 12, no. 4, pp. 1021–1029, 2018.
[23] J. Pou, S. Ceballos, G. Konstantinou, V. G. Agelidis, R. Picas, and J. Zaragoza, "Circulating current injection methods based on instantaneous information for the modular multilevel converter," *IEEE Trans. Ind. Electron.*, vol. 62, no. 2, pp. 777–788, Feb. 2015.
[24] Y. Zhu, J. Pou, and G. Konstantinou, "Impedance shaping effects and stability assessment of circulating current control schemes in modular multilevel converters," *IEEE Trans. Power Del.*, vol. 38, no. 1, pp. 666–676, Feb. 2023.
[25] J. Sun and H. Liu, "Sequence impedance modeling of modular multilevel converters," *IEEE J. Emerg. Sel. Topics Power Electron.*, vol. 5, no. 4, pp. 1427–1443, Dec. 2017.
[26] "Guide for the development of models for HVDC converters in a HVDC grid," *CIGRE Work Group B4.57*, 2014.
[27] D. Wu, G. Li, M. Javadi, A. M. Malyscheff, M. Hong, and J. N. Jiang, "Assessing impact of renewable energy integration on system strength using site-dependent short circuit ratio," *IEEE Trans. Softw. Eng.*, vol. 9, no. 3, pp. 1072–1080, Jul. 2018.
[28] M. K. Bakhshizadeh et al., "Couplings in phase domain impedance modelling of grid-connected converters," *IEEE Trans. Power Electron.*, vol. 31, no. 10, pp. 6792–6796, Oct. 2016.
[29] S. Jiang, Y. Zhu, and G. Konstantinou, "Settling-angle-based stability analysis for multiple current-controlled converters," *IEEE Trans. Power Electron.*, vol. 37, no. 11, pp. 12992–12997, Nov. 2022.
[30] G. Konstantinou, S. Ceballos, I. Gabiola, J. Pou, B. Karanayil, and V. G. Agelidis, "Flexible prototype of modular multilevel converters for experimental verification of dc transmission and multiterminal systems," in *Proc. Asian Conf. Energy, Power Transp. Electrific.*, Singapore, 2017, pp. 1–6.

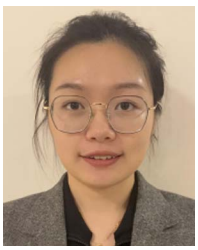

Ye Zhu (Graduate Student Member, IEEE) received the B.S. and M.E. degrees in electrical engineering from Shanghai Jiao Tong University, Shanghai, China, in 2017 and 2020, respectively. She is currently working toward the Ph.D. degree in electrical engineering with UNSW Sydney, Sydney, NSW, Australia.

Her current research interests include the modeling, analysis and control of modular multilevel converters.

Shan Jiang (Graduate Student Member, IEEE) received the B.S. and M.E. degrees in electrical engineering from Shanghai Jiao Tong University, Shanghai, China, in 2017 and 2020, respectively. He is currently working toward the Ph.D. degree in electrical engineering at UNSW Sydney, Sydney, NSW, Australia.

His current research interests include control design of power converters, and stability analysis of power electronics dominated power systems.

Josep Pou (Fellow, IEEE) received the B.S., M.S., and Ph.D. degrees in electrical engineering from the Technical University of Catalonia (UPC)-Barcelona Tech, Barcelona, Spain, in 1989, 1996, and 2002, respectively.

In 1990, he joined the faculty of UPC as an Assistant Professor, where he became an Associate Professor in 1993. From 2013 to 2016, he was a Professor with the University of New South Wales (UNSW), Sydney, Australia. He is currently a Professor with the Nanyang Technological University (NTU), Singapore, where he is Cluster Director of Power Electronics at the Energy Research Institute at NTU (ERI@N) and co-Director of the Rolls-Royce @ NTU Corporate Lab. From 2001 to 2002, and 2005 to 2006, he was a Researcher with the Center for Power Electronics Systems, Virginia Tech, Blacksburg, VA, USA. From 2012 to 2013, he was a Visiting Professor with the Australian Energy Research Institute, UNSW, Sydney. He has authored more than 470 published technical papers and has been involved in several industrial projects and educational programs in the fields of power electronics and systems. His research interests include modulation and control of power converters, multilevel converters, renewable energy, energy storage, power quality, HVdc transmission systems, and more-electrical aircraft and vessels.

Dr. Pou is an Associate Editor for IEEE JOURNAL OF EMERGING AND SELECTED TOPICS IN POWER ELECTRONICS. He was co-Editor-in-Chief and Associate Editor for IEEE TRANSACTIONS ON INDUSTRIAL ELECTRONICS. He was the recipient of the 2018 IEEE Bimal Bose Award for Industrial Electronics Applications in Energy Systems.

Georgios Konstantinou (Senior Member, IEEE) received the B.Eng. degree in electrical and computer engineering from the Aristotle University of Thessaloniki, Thessaloniki, Greece, in 2007, and the Ph.D. degree in electrical engineering from UNSW Sydney (The University of New South Wales), Australia, in 2012.

From 2013 to 2016, he was a Senior Research Associate with the University of New South Wales, Sydney, NSW, Australia, where he was part of the Australian Energy Research Institute. Since 2017, he has been with the School of Electrical Engineering and Telecommunications, UNSW Sydney, where he is currently an Associate Professor leading the real-time digital simulation (RTS@UNSW) laboratory. His research interests include multilevel converters, integration of power electronics to power systems, power electronics for renewable energy, energy storage, HVDC and MVDC applications.

Dr. Konstantinou is an Associate Editor for IEEE TRANSACTIONS ON POWER ELECTRONICS.